Open Ceramics 17 (2024) 100551

Contents lists available at ScienceDirect

Open Ceramics

journal homepage: www.sciencedirect.com/journal/open-ceramics

Ultrafast high-temperature sintering (UHS) of cerium oxide-based compound

Ahsanul Kabir [a,*], Bartłomiej Lemieszek [b], Jakub Karczewski [c], Emanuele De Bona [d], Maxim Varenik [e], Sebastian Molin [b], Mattia Biesuz [d]

[a] Institute for Manufacturing Technology of Ceramic Components and Composites, University of Stuttgart, 70569, Stuttgart, Germany
[b] Advanced Materials Center, Faculty of Electronics, Telecommunications, and Informatics, Gdańsk University of Technology, Ul. G. Narutowicza 11/12, 80-233, Gdańsk, Poland
[c] Institute of Nanotechnology and Materials Engineering, Faculty of Applied Physics and Mathematics, Gdańsk University of Technology, 80-233, Gdańsk, Poland
[d] Department of Industrial Engineering, Via Sommarive 9, 38123, Trento, Italy
[e] Department of Molecular Chemistry and Materials Science, Weizmann Institute of Science, Rehovot, 7610001, Israel

ARTICLE INFO

Handling Editor: Dr P Colombo

Keywords:
Gd-doped ceria
Ultrafast high-temperature sintering
Microstructure
Conductivity
Electrostriction

ABSTRACT

Ultrafast high-temperature sintering (UHS) is an innovative sintering technique that can densify ceramics in a few seconds, dramatically reducing the carbon footprint and firing costs. In this work, the feasibility of applying UHS in Gd-doped ceria (GDC) and GDC-Er-stabilized bismuth oxide (ESB) composite powders was investigated. At high UHS currents (22–24 A), fully dense GDC samples with a large grain size were obtained. Nonetheless, most of the GDC pellets exhibited micro/macro cracks, which were reduced by lowering the sample thickness. Interestingly, the GDC-ESB composite samples exhibit no cracks or fragmentation at all, thanks to ESB as a sintering aid. Thie samples were further characterized from an electrochemical and electromechanical point of view. The GDC-ESB material displays an ionic conductivity value of $\sim 1.5 \times 10^{-2}$ S/cm at 600 °C and frequency-stable (0.1–350 Hz) room temperature electrostriction strain coefficient of $\sim 10^{-18}$ $(m/V)^2$.

1. Introduction

The sintering of ceramics, i.e., consolidation of loose powders into a bulk solid component requires high sintering temperatures (≈2/3 T_m) usually between 1000 °C and 2000 °C, and long processing times, which account for more than 80% of the energy consumed for their production. According to recent studies, ceramics manufacturing yearly accounts for the emission of 1.3 trillion kg of CO_2 [1], giving a market value of over $100 billion per year. From a materials standpoint, such lengthy high-temperature exposures may have a detrimental impact on the microstructures of ceramics such as undesirable chemical interactions, the loss of volatile components, and abnormal grain growth [2]. Therefore, modern ceramic processing methods are pushing towards the reduction [3] of firing energy either by lowering the sintering temperature or shortening processing time. In this context, advanced sintering techniques with enhanced energy efficiency have emerged over the last few years such as fast firing [4,5], laser sintering [6], microwave sintering [7], spark plasma sintering [8], flash sintering [9,10], cold sintering [11,12], etc. To date, they have been partially established at the industrial scale. However, sintering in these methods relies on specific material characteristics such as laser and microwave absorption, solubility, and electric conductivity which limits their widespread applicability. Very recently, a novel sintering technology called ultra-fast high-temperature sintering (UHS) has been developed by Wang et al. [13]. UHS is a pressure-less sintering technique that can densify ceramic material more than 1000 times faster than conventional sintering. In this method, a green body is sandwiched between two carbon felts in an inert atmosphere. The process employs an electric current that rapidly heats the carbon felt by Joule heating and provides sufficient heat up to 10^3–10^4 °C/min, bringing the material rapidly to the sintering temperature (up to 2000+ °C) through radiation and thermal conduction [14,15]. As a result, near-full densification of the powder compacts occurs in a few seconds. Such high kinetics also provide additional benefits such as limited grain coarsening, reduced loss of volatile elements (Li/Na), and hindered inter-diffusion in multi-layered/composite ceramics [16,17]. Moreover, UHS can bring the materials to a non-equilibrium state, which may have unanticipated advantages like lowering the activation energy for densification [13], enhancing or impairing specific phase

* Corresponding author.
E-mail address: ahsanul.kabir@ifkb.uni-stuttgart.de (A. Kabir).

https://doi.org/10.1016/j.oceram.2024.100551
Received 1 December 2023; Received in revised form 27 January 2024; Accepted 1 February 2024
Available online 8 February 2024

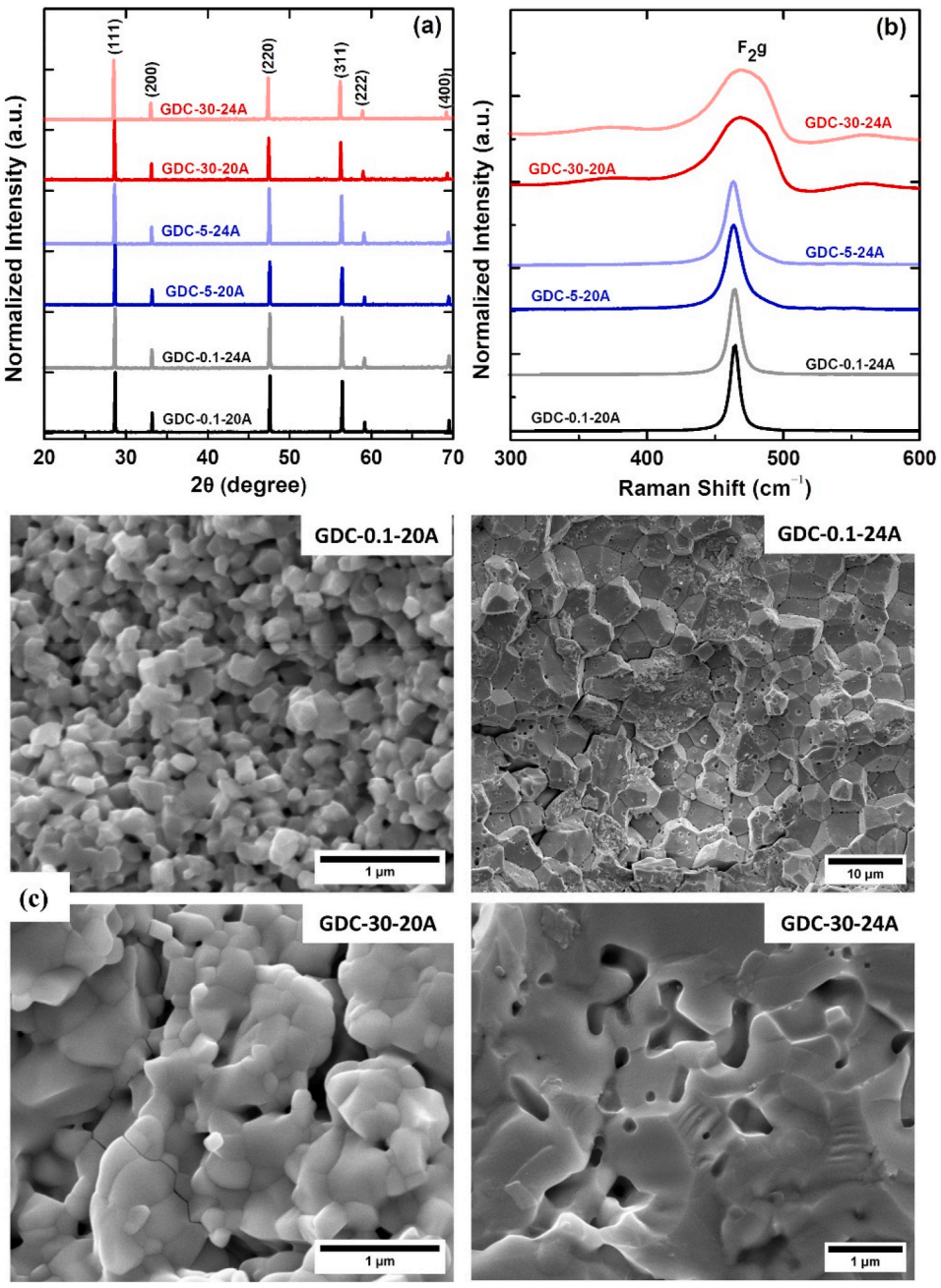

Fig. 1. (a) X-ray diffraction (XRD) patterns and (b) Raman spectra of GDC pellets, sintered via UHS. (c) SEM image of the cold-fractured surfaces of the GDC samples. GDC-0.1–24A and GDC-30-20A reveal intergranular cracks.

changes, and formation of grain boundary segregation [18,19].

So far, UHS has been explored in various ceramics compounds such as Al_2O_3 [20], Si_3N_4 [21], YSZ [13], ultra-high-temperature ceramics [19,22], high-entropy compounds [23–25] and solid-state electrolytes of LLZO/LATP [13,26] as well as samples with complex shapes [27] and large thicknesses [14,28]. However, to the best of our knowledge, there was little interest in studying ceria-based compounds (just one work in the literature [29]), a model material that is extensively used in electro-ceramics as a solid electrolyte and electrode material for solid oxide cells (SOCs) [4], catalysts [30], gas sensors [31], memristors [32], gas separation membranes [33], etc. Furthermore, unusual electromechanical activity was recently demonstrated in both thin films and bulk ceramics of ceria-derivates [34–36].

The main aim of the current work is to examine the feasibility of applying the UHS process in consolidating ceria-based ceramics with or without the addition of bismuth oxide and shedding light on essential properties such as densification behavior and microstructure evolution, electrical and electromechanical properties.

2. Experimental Procedures

2.1. Powder synthesis

Nanosized gadolinium doped ceria (GDC) powder with different compositions ($Ce_{1-x}Gd_xO_{2-\delta}$ where x = 0.01, 0.05, and 0.3) were synthesized by the co-precipitation method in an aqueous solution, as described in details elsewhere [37]. GDC and Er-stabilized Bismuth Oxide (ESB) composites were obtained using commercial 20 mol% Gd-doped ceria (GDC) powders (DC-20 K, Daiichi Kigenso Kagaku Kogyo Co., Japan) and 20 mol% Er- stabilized bismuth oxide (ESB),

synthesized by solid-state reaction [38]. For the composite, three different compositions were selected (1, 2, and 4 wt% of ESB in GDC). At first, the appropriate amount of powder was dispersed into ethanol and the dispersion was ball-milled overnight in a plastic bottle. The milling balls were then separated from the slurry and then oven-dried at 100 °C and calcined at 300 °C for 1 h in a hot plate. The powder was then gently crushed using a mortar and pestle and sieved (150 μm).

2.2. Pellet preparation

The green pellets were produced by uniaxial pressing at 200 MPa for 30 s with a diameter of 8 mm. The relative density of the green samples was ~45–50%. UHS was carried out in an Ar-filled borosilicate glass flask using graphite felt (70 × 24 × 5 mm^3). About 20 mm of the felt were clamped on both sides by two steel electrodes so the heating zone was 30 × 24 × 5 mm^3. The green sample was put into the middle of the felt which was cut by a razor blade. A DC electric current was applied stepwise (1A every 10 s, starting from 15A), to maximum currents between 18 and 24 A. After reaching the maximum current, it was held for 15 s. After that, the power was turned off which led to the fast cooling off of the sample. The total time of the sintering process was less than 5 min. The samples were mechanically polished using SIC grinding papers up to grit 2500.

2.3. Materials characterization

The bulk density of the sintered ceramics pellets was measured by Archimedes' method in a water medium at room temperature. The crystallographic phase purity was analyzed by X-ray diffraction (XRD) technique, Philips PANalytical X'Pert) with CuK_α radiation, and the Raman spectroscopy using a LabRAM Aramis equipped with an excitation laser 532 nm. The microstructure was examined by a scanning electron microscope (SEM), model FEI Quanta FEG 250 coupled with an energy dispersive x-ray spectroscopy (EDS), EDAX Genesis APEX 2i with ApolloX SDD spectrometer. The grain sizes were calculated by the linear intercept method and multiplied with a correction factor of 1.57 [39]. The electrical properties were investigated by electrochemical impedance spectroscopy (EIS) using a Solarton (1260) at a temperature between 300 and 600 °C in the frequency range of 0.05 Hz–3 MHz with an AC signal of 30 mV. The platinum paste (electrode) was applied on opposites of the pellet and fired at 700 °C for 1 h in air to ensure good contact with the platinum mesh of the setup. The EIS data were fitted employing an equivalent circuit model consisting of a resistor connected in parallel to a constant phase element and analyzed by the ZView software. The electromechanical properties were measured under ambient conditions (23 °C, relative humidity 20−55%) using a proximity sensor (Capacitance, Lion). The signal from the sensor was read by a lock-in amplifier, as explained in detail elsewhere [40,41]. The electrostrictive strain was calculated as a ratio between the field-induced displacement and the original thickness of the pellets.

3. Results and discussions

3.1. Gd doped ceria (GDC)

The synthesized powders are nanometric in size (15–30 nm), loosely agglomerated, and have no impurities (Fig. S1). The cold-pressed green GDC samples were consolidated by UHS at different currents ranging from 20A to 24A, for 15 s holding. At 20A, the predicted temperature at the felt is around 1150 °C, and with a 2A of current escalation a 100 °C increment is also anticipated [27]. At currents ≥ 22A, most of the samples show an inhomogeneous dark color (the usual color is yellowish) suggesting a partial chemical reduction of the sample (Ce^{4+} → Ce^{3+}) [42]. Discoloration has been observed previously for ceria compounds sintered in UHS or similar field-assisted sintering technologies using graphite tooling and at low oxygen partial pressure [42,43]. Thus, all the samples were post-annealed at 800 °C for 1 h in an air atmosphere. The crystallographic phase composition and microstructure of the sintered GDC samples are shown in Fig. 1. As expected, the diffraction pattern (Fig. 1a) shows a single-phase cubic fluorite structure like pure ceria (Fm-3m). Within the resolution limit of the XRD technique, no secondary phases (double fluorite) were noticed, even for the GDC-30 sample. The crystallographic phase is further confirmed by Raman spectra (Fig. 1b) and displays a sharp peak at about 460 cm^{-1} which corresponds to the F_{2g} mode of the CeO_2 fluorite structure and is ascribed to symmetrical stretching of the Ce–O bond in eightfold coordination [44,45]. With increasing dopant concentration, the peak shifts and broadens, highlighting the dissolution of the solute/dopant into the CeO_2 lattice. The extra shoulder peak at 561 cm^{-1} for the GDC-30 sample is assigned to dopant-oxygen vacancy defect clusters [46]. As shown in SEM images (Fig. 1c and Fig. S2), the samples sintered at 20A are still largely porous exhibiting the typical microstructure of the intermediate sintering stages, the grain size is submicrometric. Moreover, with increasing current to 22A/24A, densification as well as grain growth increases. Nevertheless, small pores are visible in the microstructure. The EDS elemental mapping and average grain size of the samples are listed in Figs. S3 and S4, respectively. The EDS map confirms a homogenous solid solution of GDC without any impurity phase. For GDC-0.1, the grain size increased from ~300 nm at 20 A to ~7 μm at 24 A, by nearly a factor of 20. The extremely high grain growth in such a short time strongly suggested extremely fast diffusion through the grain boundaries at 24A, which can be attributed to a reduction of the cation. It has already been reported that in fluorite-structured ceramics the energy barrier for ion migration in reducing conditions is heavily reduced [47] resulting in extraordinary grain growth [48]. The grains have a fully relaxed shape, grain boundaries are flat and reveal intergranular micro-cracks. Such an effect is attributed to the chemo-mechanical stress that is generated due to the reduction (chemical expansion) during sintering and following room temperature oxidation (chemical contraction). For ceria, micro-crack formation was typical for sintering under a reducing atmosphere and has already been reported in the works of literature [49–51]. Moreover, restricted grain growth is observed for highly doped ceria samples (GDC-5 and GDC-30) because mass diffusion is strongly limited by the dopant solute drag effect. These outcomes are exactly opposite to D. Ni et al. who showed restricted and enhanced grain growth in low and highly-doped ceria, respectively sintered under reducing conditions [52]. It is worth mentioning that oxygen partial pressure (1400 °C, for 4 h, 9% H_2–N_2, $10^{-31} < pO_2$) in their study was much lower than this work. The solute drag effect is also experiential for the sample, fabricated via conventional free sintering in the air (Fig. S5). Point to note that most of the UHS sintered samples demonstrated micro and/or macro cracks and were highly sensitive to fragmentation (Fig. S6), thus they were not subjected to further property characterization. Moreover, by decreasing the sample thickness, fragmentation was avoided and the number of microcracks was reduced to a minimum.

3.2. Gd doped ceria (GDC) and Er-stabilized bismuth oxide (ESB) composite

An alternative way to mitigate cracking problems was to add a highly functional bismuth oxide phase in GDC. The bismuth oxide additives melt during sintering. Thus, the volume (chemical) expansion from Ce^{4+} to Ce^{3+} is accommodated by the liquid phase and hinders cracking. Recent studies also demonstrate that the introduction of bismuth oxide in ceria-based compounds significantly increases electrostrictive, ionic conductivity, and mechanical properties [53,54]. Among all stabilized bismuth oxides, 20 mol% Er-stabilized bismuth oxide (ESB) exhibits the highest conductivity [55] and stabilized bismuth oxide is also a non-classical electrostrictor [40]. The sintering protocol of the ESB-GDC composite was the same as the pure GDC as mentioned above. These samples were also post-annealed at 800 °C for 1 h in air. The as-sintered

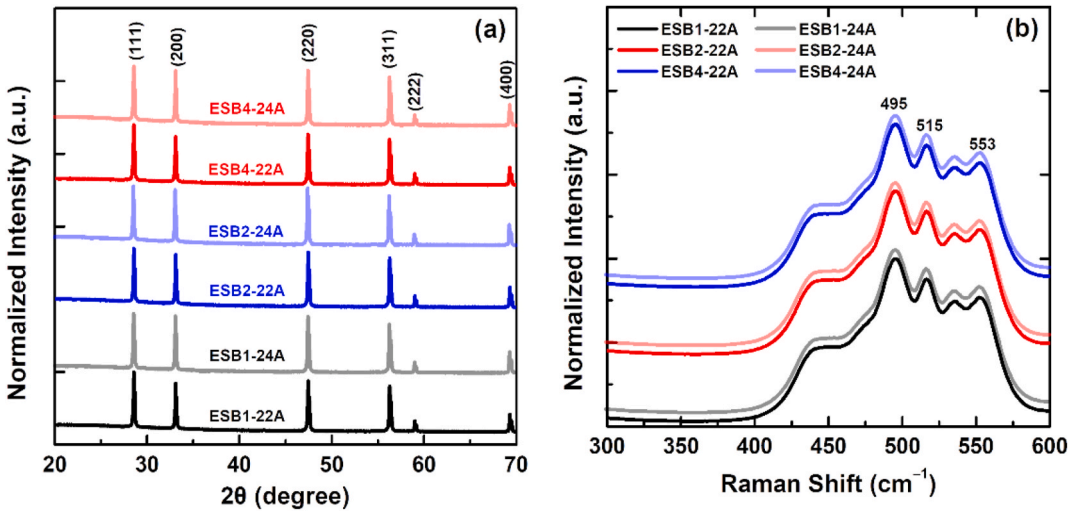

Fig. 2. (a) X-ray diffraction (XRD) patterns and (b) Raman spectra of GDC-ESB composite pellets, sintered via UHS method employing 13V-22/24A.

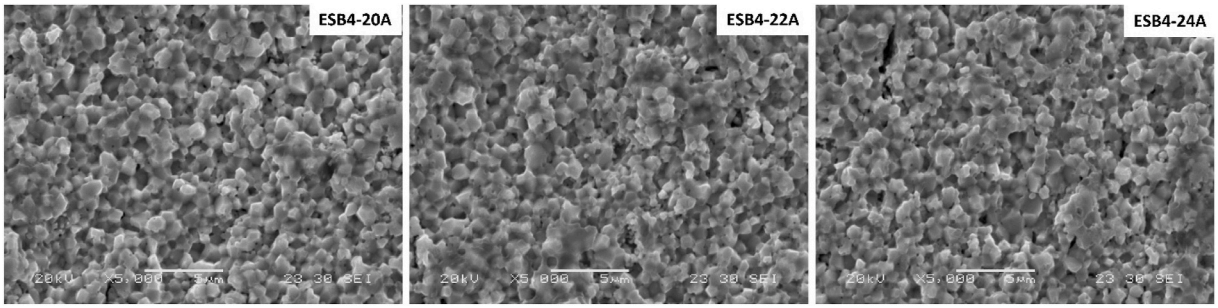

Fig. 3. Scanning electron microscope (SEM) image of the cold-fractured surfaces of the GDC-ESB composite (4 wt% ESB in GDC) samples, sintered at 20–24A.

GDC-ESB composite pellet was crack-free and mechanically stable (Fig. S7). Visual inspection exhibited that compared with pure GDC, the ESB-GDC compound has a relatively high shrinkage. It was reported for conventional sintering that Bi_2O_3 additives with concentration ≥0.5 wt % have a factor of 2–5 higher shrinkage rate compared to pure-GDC one, significantly impacting the sintering mechanism [56]. The bulk density

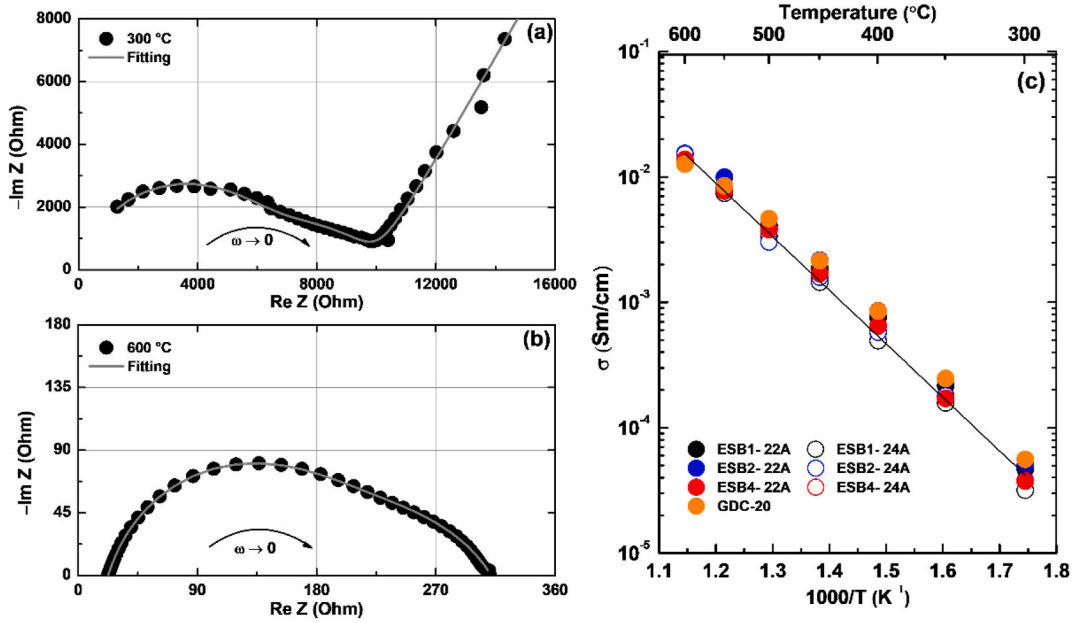

Fig. 4. (a–b) Representation of the impedance spectra i.e. Nyquist plot (Re Z vs Im Z) at temperatures of 300 and 600 °C of ESB1-24A pellet, measured in synthetic air with Pt electrode. Impedance was also performed on additional samples to confirm the reproducibility of the results. (c) Arrhenius plot for the estimation of the temperature-dependent total electrical conductivity of the GDC-ESB composite samples.

of the sample is listed in Table S1. The crystallographic phase purity and micrographs of the fracture surfaces are reported in Fig. 2. As expected, no crystal planes other than cubic fluorite structures like pure CeO_2 are observed in the XRD diffraction pattern (Fig. 2a). The peak intensity at (200) and (400) crystalline planes are unexpectedly higher as compared to the UHS sintered GDC compound, albeit the reason for this is unclear. A possible explanation might be the development of some texture which is not uncommon in liquid phase sintering, occurs due to grain re-arrangement and dissolve precipitation stages. Raman spectra (Fig. 2b) show dominant peaks around the 495, 515, and 553 bands, attributed to γ-Bi_2O_3 phase (space group, I23) [57]. The shoulder peak near ~445 cm^{-1} Raman band resembles the F_{2g} mode of the GDC.

The exemplary SEM images of the sintered samples are demonstrated in Fig. 3 and Fig. S8, further confirming a good level of densification behavior. ESB has a melting point of around ~850 °C, therefore it melts during sintering, enabling rapid densification by liquid phase sintering. Since the solubility limit of cubic-structured Bi_2O_3 in GDC was found to be about 0.8 wt % [58], ESB is expected to be present at the grain boundaries or triple points. As observed, the grain structures are well-homogenized having equiaxed grains whose size is between 1.8 and 2.0 μm and could be attributed to the intermediate-stage sintering, i.e., in which the samples are ≥95% dense and closed porosity [56].

Gil et al. claimed that the retarded or not promoting grain growth in ESB-GDC composite can be assumed to be due to poor wetting properties of the formed liquid phase [56]. Zhao and coworkers also disclosed similar results showing that the addition of Bi_2O_3 did not considerably affect the grain growth kinetics of the doped ceria compounds [59]. Since UHS is occurring at extremely high temperatures but for a short time, a few Bi_2O_3 contents can evaporate (sublimation temperature is around 1000 °C [60]). At 22A–24A, the predicted temperature of the felt is around 1250–1350 °C as mentioned above [27]. The elemental analysis obtained by EDS shown in Fig. S9, confirms a loss of Bi from the samples and local segregation at the triple point.

The electrical properties of the samples are measured using impedance spectroscopy in the air at the temperature of 300–600 °C. Fig. 4a and b exemplifies a typical EIS spectrum i.e., a Nyquist plot of ESB1-24A sample at two different temperatures. At 300 °C, the sample exhibits a slightly deformed single semicircle. Typically, ceramics oxide exhibits two well-resolved semi-circles: at high and low frequencies, corresponding to the transport phenomena in the bulk/grain interior and grain boundaries, respectively [4,43]. A single semicircle is often observed for nanocrystalline ceramics and can be attributed to overlapped bulk and grain boundary contribution [61]. Moreover, its characteristic frequency value (~1 MHz) suggests that the semicircle is probably dominated by bulk contribution (Bode plots Fig. S10). Its capacitance value (4.5×10^{-9} F) is roughly two orders of magnitude higher than the expected bulk value. With increasing temperature, the superimposed contribution of bulk and grain boundary decreases significantly and a single semicircle due to electrolyte-electrode interfaces is observed because the relaxation frequency is shifted towards high frequencies at a higher temperature [62,63]. This advocates that ionic conductivity is a thermally activated process and it increases as the relaxation time response of the oxygen ion decreases [64,65]. The temperature-dependent total electrical (ionic) conductivity (σ) of the samples is plotted in an Arrhenius relationship in Fig. 4c. The Arrhenius equation follows, $\sigma T = \sigma_0 \exp\left(\frac{-E_a}{kT}\right)$ where σ_0, k, E_a denotes the pre-exponential factor, Boltzmann constant, and activation energy of long-range oxygen ion migration respectively. The conductivity value conductivity is similar among the investigated samples and conventionally sintered reference GDC-20. The conductivity value at 600 °C is $\sim 1.5 \times 10^{-2}$ S/cm and is in line with previous reports [58,66]. The activation energy is obtained from the slope of the straight line. All samples have a similar activation energy of approx. ~0.85 eV and in good agreement with the literature data [37]. In summary, UHS allowed to get in a few minutes defect-free and well-densified ESB-GDC composites with electrochemical properties substantially analogous to those of electrolytes obtained by slow conventional firing.

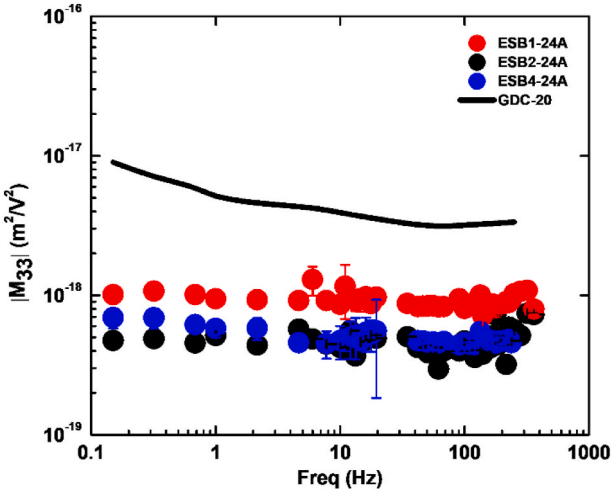

Fig. 5. Electrostriction strain coefficient (M_{33}) as a function of applied AC frequency. The data is compared with 20 mol% Gd-doped ceria [67].

The electromechanical properties of the sample were measured at room temperature and illustrated in Fig. 5. The investigated compound responds at the second harmonic of the applied electric field and contracts in the direction of the applied electric field, confirming its electrostriction behavior [68,69]. They exhibit longitudinal strain that agrees with previous reports of the GDC and other doped ceria compounds [70]. The electrostrictive strain coefficient M_{33} value was high in the ESB1-24A sample and interestingly, it was found that M_{33} decreases with ESB concentration. Although the magnitude of M_{33} is one order of value lower than GDC-20 [67], these compounds do not display Debye-type frequency-dependent strain relaxation. Frequency-associated strain relaxation is typical for Gd-doped ceria and is described in various previous reports [71,72]. The M_{33} value at 100 Hz in the ESB1-24A sample is 10^{-18} $(m/V)^2$ is still one order of magnitude larger than the Newnham scaling law prediction and gigantic in nature.

4. Conclusion

In this work, UHS was applied to sinter pure GDC and GDC-ESB composite ceramics. The entire sintering process took less than 5 min, including heating, dwelling, and cooling steps which are at least 100 times shorter than conventional firing cycles of ceria-based ceramics. The pure GDC ceramics showed macrocracks and fragmentation due to chemical reduction during sintering. The addition of ESB reduces the cracking problem. In both types of samples, densification and grain growth increase with increasing the applied UHS current. The addition of ESB did not change the electrical properties, however, the electromechanical response generally decreased with ESB addition. Despite this reduction, the M_{33} coefficient was found to be gigantic for the GDC sample doped with 1 wt% of ESB and UHSed under 24 A. Interestingly, the electromechanical properties are extremely robust and frequency-stable in the 0.1–400 Hz frequency range.

Declaration of competing interest

The authors declare that they have no known competing financial interests or personal relationships that could have appeared to influence the work reported in this paper.

Acknowledgment

This work was supported by the PRIME programme of the German Academic Exchange Service (DAAD) with funds from the German Federal Ministry of Education and Research (BMBF) and JECS Trust-Fund Contract-2021275. The research was also supported by the Italian Ministry for University and Research (MUR) through the "Departments of Excellence 2023–27" program (L.232/2016) - awarded to the Department of Industrial Engineering of the University of Trento."

Appendix A. Supplementary data

Supplementary data to this article can be found online at https://doi.org/10.1016/j.oceram.2024.100551.

References

[1] K.J. Holmes, E. Zeitler, M. Kerxhalli-Kleinfield, R. DeBoer, Scaling deep decarbonization technologies, Earth's Future 9 (2021), https://doi.org/10.1029/2021EF002399.
[2] M. Biesuz, S. Grasso, V.M. Sglavo, What's new in ceramics sintering? A short report on the latest trends and future prospects, Curr. Opin. Solid State Mater. Sci. 24 (2020) 100868, https://doi.org/10.1016/j.cossms.2020.100868.
[3] R. Chaim, G. Chevallier, A. Weibel, C. Estournès, Grain growth during spark plasma and flash sintering of ceramic nanoparticles : a review, J. Mater. Sci. 53 (2018) 3087–3105, https://doi.org/10.1007/s10853-017-1761-7.
[4] V. Esposito, E. Traversa, Design of electroceramics for solid oxides fuel cell applications: playing with ceria, J. Am. Ceram. Soc. 91 (2008) 1037–1051, https://doi.org/10.1111/j.1551-2916.2008.02347.x.
[5] M. Biesuz, L. Spiridigliozzi, M. Frasnelli, G. Dell'Agli, V.M. Sglavo, Rapid densification of Samarium-doped Ceria ceramic with nanometric grain size at 900–1100 °C, Mater. Lett. 190 (2017) 17–19, https://doi.org/10.1016/j.matlet.2016.12.132.
[6] B. Qian, Z. Shen, Laser sintering of ceramics, Journal of Asian Ceramic Societies 1 (2013) 315–321, https://doi.org/10.1016/j.jascer.2013.08.004.
[7] J.D. Katz, Microwave sintering of ceramics, Annu. Rev. Mater. Sci. 22 (1992) 153–170, https://doi.org/10.1146/annurev.ms.22.080192.001101.
[8] O. Guillon, J. Gonzalez-Julian, B. Dargatz, T. Kessel, G. Schierning, J. Räthel, M. Herrmann, Field-assisted sintering technology/spark plasma sintering: mechanisms, materials, and technology developments, Adv. Eng. Mater. 16 (2014) 830–849, https://doi.org/10.1002/adem.201300409.
[9] M. Biesuz, V.M. Sglavo, Flash sintering of ceramics, J. Eur. Ceram. Soc. 39 (2019) 115–143, https://doi.org/10.1016/j.jeurceramsoc.2018.08.048.
[10] M. Yu, S. Grasso, R. Mckinnon, T. Saunders, M.J. Reece, Review of flash sintering: materials, mechanisms and modelling, Adv. Appl. Ceram. 116 (2017) 24–60, https://doi.org/10.1080/17436753.2016.1251051.
[11] J. Guo, R. Floyd, S. Lowum, J.-P. Maria, T. Herisson de Beauvoir, J.-H. Seo, C. A. Randall, Cold sintering: progress, challenges, and future opportunities, Annu. Rev. Mater. Res. 49 (2019) 275–295, https://doi.org/10.1146/annurev-matsci-070218-010041.
[12] A. Galotta, V.M. Sglavo, The cold sintering process: a review on processing features, densification mechanisms and perspectives, J. Eur. Ceram. Soc. 41 (2021) 1–17, https://doi.org/10.1016/j.jeurceramsoc.2021.09.024.
[13] C. Wang, W. Ping, Q. Bai, H. Cui, R. Hensleigh, R. Wang, A.H. Brozena, Z. Xu, J. Dai, Y. Pei, C. Zheng, G. Pastel, J. Gao, X. Wang, H. Wang, J.-C. Zhao, B. Yang, X. Rayne, Zheng, J. Luo, Y. Mo, B. Dunn, L. Hu, A general method to synthesize and sinter bulk ceramics in seconds, Science 368 (2020) 521–526, https://doi.org/10.1126/science.aaz7681, 1979.
[14] F. Zuo, Q. Wang, Z.-Q. Yan, M. Kermani, S. Grasso, G.-L. Nie, B.-B. Jiang, F.-P. He, H.-T. Lin, L.-G. Wang, Upscaling Ultrafast High-Temperature Sintering (UHS) to consolidate large-sized and complex-shaped ceramics, Scripta Mater. 221 (2022) 114973, https://doi.org/10.1016/j.scriptamat.2022.114973.
[15] M. Kermani, D. Zhu, J. Li, J. Wu, Y. Lin, Z. Dai, C. Hu, S. Grasso, Ultra-fast high-temperature sintering (UHS) of translucent alumina, Open Ceramics 9 (2022) 100202, https://doi.org/10.1016/j.oceram.2021.100202.
[16] R. Wang, Q. Dong, C. Wang, M. Hong, J. Gao, H. Xie, M. Guo, W. Ping, X. Wang, S. He, J. Luo, L. Hu, High-temperature ultrafast sintering: exploiting a new kinetic region to fabricate porous solid-state electrolyte scaffolds, Adv. Mater. 33 (2021), https://doi.org/10.1002/adma.202100726.
[17] H. Zhang, R. Dubey, M. Inniger, F. Okur, R. Wullich, A. Parrilli, D.T. Karabay, A. Neels, K.V. Kravchyk, M.V. Kovalenko, Ultrafast-sintered self-standing LLZO membranes for high energy density lithium-garnet solid-state batteries, Cell Rep Phys Sci 4 (2023) 101473, https://doi.org/10.1016/j.xcrp.2023.101473.
[18] T.P. Mishra, S. Wang, C. Lenser, D. Jennings, M. Kindelmann, W. Rheinheimer, C. Broeckmann, M. Bram, O. Guillon, Ultra-fast high-temperature sintering of strontium titanate, Acta Materialia 231 (2022) 117918, https://doi.org/10.1016/j.actamat.2022.117918.
[19] E. De Bona, C. Manière, V.M. Sglavo, M. Biesuz, Ultrafast high-temperature sintering (UHS) of ZrB2-based materials, J. Eur. Ceram. Soc. 44 (2024) 567–573, https://doi.org/10.1016/j.jeurceramsoc.2023.09.007.
[20] M. Kermani, J. Dong, M. Biesuz, Y. Linx, H. Deng, V.M. Sglavo, M.J. Reece, C. Hu, S. Grasso, Ultrafast high-temperature sintering (UHS) of fine grained α-Al2O3, J. Eur. Ceram. Soc. 41 (2021) 6626–6633, https://doi.org/10.1016/j.jeurceramsoc.2021.05.056.
[21] R.-X. Luo, M. Kermani, Z.-L. Guo, J. Dong, C.-F. Hu, F. Zuo, S. Grasso, B.-B. Jiang, G.-L. Nie, Z.-Q. Yan, Q. Wang, Y.-L. Gan, F.-P. He, H.-T. Lin, Ultrafast high-temperature sintering of silicon nitride: a comparison with the state-of-the-art techniques, J. Eur. Ceram. Soc. 41 (2021) 6338–6345, https://doi.org/10.1016/j.jeurceramsoc.2021.06.021.
[22] R.-F. Guo, H.-R. Mao, P. Shen, Ultra-fast high-temperature synthesis and densification of high-entropy diborides and diboride-carbide ceramics, J. Eur. Ceram. Soc. 43 (2023) 5763–5773, https://doi.org/10.1016/j.jeurceramsoc.2023.05.042.
[23] L. Spiridigliozzi, G. Dell'Agli, S. Esposito, P. Rivolo, S. Grasso, V.M. Sglavo, M. Biesuz, Ultra-fast high-temperature sintering (UHS) of Ce0.2Zr0.2Y0.2Gd0.2La0.2O2−δ fluorite-structured entropy-stabilized oxide (F-ESO), Scripta Mater. 214 (2022) 114655, https://doi.org/10.1016/j.scriptamat.2022.114655.
[24] H.-R. Mao, E.-T. Dong, S.-B. Jin, X.-M. Qiu, P. Shen, Ultrafast high-temperature synthesis and densification of high-entropy carbides, J. Eur. Ceram. Soc. 42 (2022) 4053–4065, https://doi.org/10.1016/j.jeurceramsoc.2022.03.054.
[25] F. Ye, F. Meng, T. Luo, H. Qi, Ultrafast high-temperature sintering of high-entropy (La0.2Nd0.2Sm0.2Eu0.2Gd0.2)2Hf2O7 ceramics with fluorite structure, Ceram. Int. 48 (2022) 35649–35654, https://doi.org/10.1016/j.ceramint.2022.09.041.
[26] A. Kern, P.J. McGinn, Ultrafast high-temperature sintering of Li7La3Zr1.75Nb0.25Al0.15O12 (LLZO), J. Eur. Ceram. Soc. 42 (2022) 7501–7507, https://doi.org/10.1016/j.jeurceramsoc.2022.08.054.
[27] S. Bhandari, C. Manière, F. Sedona, E. De Bona, V.M. Sglavo, P. Colombo, L. Fambri, M. Biesuz, G. Franchin, Ultra-rapid debinding and sintering of additively manufactured ceramics by ultrafast high-temperature sintering, J. Eur. Ceram. Soc. 44 (2024), https://doi.org/10.1016/j.jeurceramsoc.2023.08.040.
[28] J. Wu, M. kermani, D. Zhu, J. Li, Y. Lin, C. Hu, S. Grasso, Carbon free ultra-fast high temperature sintering of translucent zirconia, Scripta Mater. 210 (2022) 114476, https://doi.org/10.1016/j.scriptamat.2021.114476.
[29] A. Alemayehu, M. Biesuz, K.Y. Javan, A. Tkach, P.M. Vilarinho, V.M. Sglavo, V. Tyrpekl, Ultrafast high-temperature sintering of gadolinia-doped ceria, J. Eur. Ceram. Soc. 43 (2023) 4837–4843, https://doi.org/10.1016/j.jeurceramsoc.2023.04.025.
[30] A. Dankeaw, F. Gualandris, R.H. Silva, K. Norrman, M. Gudik-Sørensen, K. K. Hansen, B. Ksapabutr, V. Esposito, D. Marani, Amorphous saturated cerium–tungsten–titanium oxide nanofiber catalysts for NO $_x$ selective catalytic reaction, New J. Chem. 42 (2018) 9501–9509, https://doi.org/10.1039/C8NJ00752G.
[31] T.S. Stefanik, H.L. Tuller, Ceria-based gas sensors, J. Eur. Ceram. Soc. 21 (2001) 1967–1970, https://doi.org/10.1016/S0955-2219(01)00152-2.
[32] R. Schmitt, A. Nenning, O. Kraynis, R. Korobko, A.I. Frenkel, I. Lubomirsky, S. M. Haile, J.L.M. Rupp, A review of defect structure and chemistry in ceria and its solid solutions, Chem. Soc. Rev. 49 (2020) 554–592, https://doi.org/10.1039/C9CS00588A.
[33] A. Kaiser, S.P. Foghmoes, G. Pećanac, J. Malzbender, C. Chatzichristodoulou, J. A. Glasscock, D. Ramachandran, D.W. Ni, V. Esposito, M. Søgaard, P. V. Hendriksen, Design and optimization of porous ceramic supports for asymmetric ceria-based oxygen transport membranes, J. Membr. Sci. 513 (2016) 85–94, https://doi.org/10.1016/j.memsci.2016.04.016.
[34] J.K. Han, A. Kabir, V.B. Tinti, S. Santucci, D.S. Song, S.Y. Kim, W. Song, E. Kim, S. D. Bu, F. Kern, D.Z. de Florio, V. Esposito, Enhanced electromechanical properties in low-temperature gadolinium-doped ceria composites with low-dimensional carbon allotropes, J Mater Chem A Mater 10 (2022) 4024–4031, https://doi.org/10.1039/D1TA10854A.
[35] E. Wachtel, A.I. Frenkel, I. Lubomirsky, Anelastic and electromechanical properties of doped and reduced ceria, Adv. Mater. 30 (2018) 1707455, https://doi.org/10.1002/adma.201707455.
[36] R. Korobko, A. Patlolla, A. Kossoy, E. Wachtel, H.L. Tuller, A.I. Frenkel, I. Lubomirsky, Giant electrostriction in Gd-doped ceria, Adv. Mater. 24 (2012) 5857–5861, https://doi.org/10.1002/adma.201202270.
[37] A. Kabir, J. Kyu Han, B. Merle, V. Esposito, The role of oxygen defects on the electro-chemo-mechanical properties of highly defective gadolinium doped ceria, Mater. Lett. 266 (2020) 127490, https://doi.org/10.1016/j.matlet.2020.127490.
[38] S. Sanna, V. Esposito, C. Graves, J. Hjelm, J.W. Andreasen, N. Pryds, Structural instability and electrical properties in epitaxial Er2O3-stabilized Bi2O3 thin films, Solid State Ionics 266 (2014) 13–18, https://doi.org/10.1016/j.ssi.2014.08.004.
[39] M.I. Mendelson, Average grain size in polycrystalline ceramics, J. Am. Ceram. Soc. 52 (1969) 443–446, https://doi.org/10.1111/j.1151-2916.1969.tb11975.x.
[40] N. Yavo, A.D. Smith, O. Yeheskel, S. Cohen, R. Korobko, E. Wachtel, P.R. Slater, I. Lubomirsky, Large nonclassical electrostriction in (Y, Nb)-Stabilized δ -Bi $_2$ O $_3$, Adv. Funct. Mater. 26 (2016) 1138–1142, https://doi.org/10.1002/adfm.201503942.
[41] M. Varenik, J.C. Nino, E. Wachtel, S. Kim, S.R. Cohen, I. Lubomirsky, Trivalent dopant size influences electrostrictive strain in ceria solid solutions, ACS Appl. Mater. Interfaces 13 (2021) 20269–20276, https://doi.org/10.1021/acsami.0c20810.
[42] A. Kabir, S. Colding-Jørgensen, S. Molin, V. Esposito, Electrical conductivity of nanostructured acceptor-doped ceria fabricated by spark plasma sintering (SPS), Mater. Lett. 279 (2020) 128513, https://doi.org/10.1016/j.matlet.2020.128513.
[43] U. Anselmi-Tamburini, F. Maglia, G. Chiodelli, A. Tacca, G. Spinolo, P. Riello, S. Bucella, Z.A. Munir, Nanoscale effects on the ionic conductivity of highly doped

bulk nanometric cerium oxide, Adv. Funct. Mater. 16 (2006) 2363–2368, https://doi.org/10.1002/adfm.200500415.
[44] V. Chierchia, H. Zhang, M. Bortolotti, A. Chiappini, G.D. Sorarù, V. Esposito, M. Biesuz, Solid solution enhanced electrostriction in the YSZ-GDC system, Open Ceramics 9 (2022) 100206, https://doi.org/10.1016/j.oceram.2021.100206.
[45] A. Banerji, V. Grover, V. Sathe, S.K. Deb, A.K. Tyagi, system: unraveling of microscopic features by Raman spectroscopy, Solid State Commun. 149 (2009) 1689–1692, https://doi.org/10.1016/j.ssc.2009.06.045.
[46] S.A. Acharya, V.M. Gaikwad, V. Sathe, S.K. Kulkarni, Influence of gadolinium doping on the structure and defects of ceria under fuel cell operating temperature, Appl. Phys. Lett. 104 (2014), 113508, doi:10.1063/1.4869116.
[47] Y. Dong, Redox enhanced slow ion kinetics in oxide ceramics, J. Am. Ceram. Soc. 107 (2024) 1905–1916, https://doi.org/10.1111/jace.19441.
[48] Y. Dong, H. Wang, I. Chen, Electrical and hydrogen reduction enhances kinetics in doped zirconia and ceria: I. Grain growth study, J. Am. Ceram. Soc. 100 (2017) 876–886.
[49] Y. Zhou, The influence of redox reaction of the sintering of cerium oxide, J. Mater. Synth. Process. 6 (1998) 411–414, https://doi.org/10.1023/A:1021833022868.
[50] Z. He, H. Yuan, J.A. Glasscock, C. Chatzichristodoulou, J.W. Phair, A. Kaiser, S. Ramousse, Densification and grain growth during early-stage sintering of Ce0.9Gd0.1O1.95−δ in a reducing atmosphere, Acta Mater. 58 (2010) 3860–3866, https://doi.org/10.1016/j.actamat.2010.03.046.
[51] V. Esposito, D.W. Ni, Z. He, W. Zhang, A.S. Prasad, J.A. Glasscock, C. Chatzichristodoulou, S. Ramousse, A. Kaiser, Enhanced mass diffusion phenomena in highly defective doped ceria, Acta Mater. 61 (2013) 6290–6300, https://doi.org/10.1016/j.actamat.2013.07.012.
[52] D.W. Ni, D.Z. de Florio, D. Marani, A. Kaiser, V.B. Tinti, V. Esposito, Effect of chemical redox on Gd-doped ceria mass diffusion, J Mater Chem A Mater 3 (2015) 18835–18838, https://doi.org/10.1039/C5TA05537G.
[53] Y.-P. Fu, C.-W. Tseng, P.-C. Peng, Effect of bismuth addition on the electrical conductivity of gadolinium-doped ceria ceramics, J. Eur. Ceram. Soc. 28 (2008) 85–90, https://doi.org/10.1016/j.jeurceramsoc.2007.05.002.
[54] H. Zhang, N. Pryds, D.-S. Park, N. Gauquelin, S. Santucci, D.V. Christensen, D. Jannis, D. Chezganov, D.A. Rata, A.R. Insinga, I.E. Castelli, J. Verbeeck, I. Lubomirsky, P. Muralt, D. Damjanovic, V. Esposito, Atomically engineered interfaces yield extraordinary electrostriction, Nature 609 (2022) 695–700, https://doi.org/10.1038/s41586-022-05073-6.
[55] N. Jaiswal, B. Gupta, D. Kumar, O. Parkash, Effect of addition of erbium stabilized bismuth oxide on the conductivity of lanthanum doped ceria solid electrolyte for IT-SOFCs, J. Alloys Compd. 633 (2015) 174–182, https://doi.org/10.1016/j.jallcom.2014.12.243.
[56] V. Gil, J. Tartaj, C. Moure, P. Duran, Effect of Bi2O3 addition on the sintering and microstructural development of gadolinia-doped ceria ceramics, J. Eur. Ceram. Soc. 27 (2007) 801–805, https://doi.org/10.1016/j.jeurceramsoc.2006.04.011.
[57] O. Depablos-Rivera, A. Martínez, S.E. Rodil, Interpretation of the Raman spectra of bismuth oxide thin films presenting different crystallographic phases, J. Alloys Compd. 853 (2021) 157245, https://doi.org/10.1016/j.jallcom.2020.157245.
[58] G. Accardo, L. Spiridigliozzi, G. Dell'Agli, S.P. Yoon, D. Frattini, Morphology and structural stability of bismuth-gadolinium Co-doped ceria electrolyte nanopowders, Inorganics (Basel) 7 (2019) 118, https://doi.org/10.3390/inorganics7100118.
[59] W. Zhao, S. An, L. Ma, Processing and characterization of Bi2O3 and Sm2O3 codoped CeO2 electrolyte for intermediate-temperature solid oxide fuel cell, J. Am. Ceram. Soc. 94 (2011) 1496–1502, https://doi.org/10.1111/j.1551-2916.2010.04270.x.
[60] H. Lee, J. Park, Y. Lim, Y.-B. Kim, Lowering the sintering temperature of a gadolinia-doped ceria functional layer using a layered Bi2O3 sintering aid for solid oxide fuel cells, Ceram. Int. 48 (2022) 2865–2871, https://doi.org/10.1016/j.ceramint.2021.10.076.
[61] A. Kabir, S. Santucci, N. Van Nong, M. Varenik, I. Lubomirsky, R. Nigon, P. Muralt, V. Esposito, Effect of oxygen defects blocking barriers on gadolinium doped ceria (GDC) electro-chemo-mechanical properties, Acta Mater. 174 (2019) 53–60, https://doi.org/10.1016/j.actamat.2019.05.009.
[62] C. Ahamer, A.K. Opitz, G.M. Rupp, J. Fleig, Revisiting the temperature dependent ionic conductivity of yttria stabilized zirconia (YSZ), J. Electrochem. Soc. 164 (2017) F790–F803, https://doi.org/10.1149/2.0641707jes.
[63] M. Gupta, S.C. Shirbhate, O.v. Rambadey, S.A. Acharya, P.R. Sagdeo, Temperature-dependent delocalization of oxygen vacancies in La-substituted CeO $_2$, ACS Appl. Energy Mater. 5 (2022) 9759–9769, https://doi.org/10.1021/acsaem.2c01442.
[64] Sk Anirban, A. Dutta, Revisiting ionic conductivity of rare earth doped ceria: dependency on different factors, Int. J. Hydrogen Energy 45 (2020) 25139–25166, https://doi.org/10.1016/j.ijhydene.2020.06.119.
[65] E. Gager, J.C. Nino, Processing, phase stability, and conductivity of multication-doped ceria, Inorganics (Basel) 11 (2023) 299, https://doi.org/10.3390/inorganics11070299.
[66] V. Gil, C. Moure, P. Duran, J. Tartaj, Low-temperature densification and grain growth of Bi2O3-doped-ceria gadolinia ceramics, Solid State Ionics 178 (2007) 359–365, https://doi.org/10.1016/j.ssi.2007.02.002.
[67] M. Varenik, J.C. Nino, E. Wachtel, S. Kim, O. Yeheskel, N. Yavo, I. Lubomirsky, Dopant concentration controls quasi-static electrostrictive strain response of ceria ceramics, ACS Appl. Mater. Interfaces 12 (2020) 39381–39387, https://doi.org/10.1021/acsami.0c07799.
[68] R.E. Newnham, V. Sundar, R. Yimnirun, J. Su, Q.M. Zhang, Electrostriction: nonlinear electromechanical coupling in solid dielectrics, J. Phys. Chem. B 101 (1997) 10141–10150, https://doi.org/10.1021/jp971522c.
[69] A. Kabir, V. Buratto Tinti, M. Varenik, I. Lubomirsky, V. Esposito, Electromechanical dopant–defect interaction in acceptor-doped ceria, Mater Adv 1 (2020) 2717–2720, https://doi.org/10.1039/D0MA00563K.
[70] H. Zhang, M. Vasiljevic, A. Bergne, D. Park, A.R. Insinga, S. Yun, V. Esposito, N. Pryds, Engineering of electromechanical oxides by symmetry breaking, Adv Mater Interfaces 10 (2023), https://doi.org/10.1002/admi.202300083.
[71] N. Yavo, O. Yeheskel, E. Wachtel, D. Ehre, A.I. Frenkel, I. Lubomirsky, Relaxation and saturation of electrostriction in 10 mol% Gd-doped ceria ceramics, Acta Mater. 144 (2018) 411–418, https://doi.org/10.1016/j.actamat.2017.10.056.
[72] A. Kabir, J.R. Bowen, M. Varenik, I. Lubomirsky, V. Esposito, Enhanced electromechanical response in Sm and Nd Co-doped ceria, Materialia (Oxf) 12 (2020) 100728, https://doi.org/10.1016/j.mtla.2020.100728.